Ceramics International 52 (2026) 21303–21316

Contents lists available at ScienceDirect

Ceramics International

journal homepage: www.elsevier.com/locate/ceramint

Sintering of wet-processed simulated Mars regolith slurries shaped using conventional and laser-induced slip casting (LIS)

Mariano Casu [a,b], Jonathan Bahr [b], Rafael Kleba-Ehrhardt [b], Thomas Mühler [c], Martin Schwentenwein [d], Ralf Feyerherm [e], Roberto Orrù [a], Giacomo Cao [a], Aleksander Gurlo [b], David Karl [b,f,*]

[a] Department of Mechanical, Chemical, and Materials Engineering, Research Unit of the National Interuniversity Consortium of Materials Science and Technology (INSTM), University of Cagliari, via Marengo 2, 09123 Cagliari, Italy
[b] Technische Universitaet Berlin, Faculty III Process Sciences, Institute of Materials Science and Technology, Chair of Advanced Ceramic Materials, Straße des 17. Juni 135, Berlin, 10623, Germany
[c] QEP3D GmbH, Gebäude 101, Ruhlsdorfer Str. 95, 14532 Stahnsdorf, Germany
[d] Lithoz GmbH, Mollardgasse 85a/2/64-69, 1060 Vienna, Austria
[e] Institute Quantum Phenomena in Novel Materials, Helmholtz-Zentrum Berlin für Materialien und Energie GmbH, Hahn-Meitner-Platz 1, Berlin, 14109, Germany
[f] Center for Space Resources, Colorado School of Mines, 1310 Maple St, Golden, 80401, Colorado, USA

ARTICLE INFO

Handling Editor: Dr P. Vincenzini

Keywords:
Space resources
ISRU
Martian regolith simulants
Laser induced slip casting
LIS
Sintering
Compressive strength
Magnetic properties

ABSTRACT

In the framework of the future manned exploration of planet Mars, the availability of efficient manufacturing techniques for the in-situ exploitation of regolith represents a key target. In this regard, the newly developed Laser Induced Slip-Casting (LIS) technique is investigated in this work, starting from 100% in-situ available materials, as an additive manufacturing route. For the sake of comparison, traditional Slip-Casting (SC) was also employed.

The use of clay-containing (2.5 wt%) materials and a Martian saltwater simulant as dispersion medium led to compact green bodies for both LIS and SC technologies. The obtained parts, after being characterized for their thermal stability both in oxidizing and inert conditions, have been sintered to produce dense specimens, with the best results observed operating at 1190 °C for 3h holding time in air, and 1180 °C for 3h in simulated Martian atmosphere. Compositional and magnetic analyses revealed different phase transformations occurring during the thermal treatments, i.e., Magnetite or Hematite formation, indicating that different phenomena occur in air and Martian atmosphere conditions. The modest compressive strength of the LIS-printed green bodies (about 0.9 MPa) can be significantly improved after sintering (about 100 MPa), obtaining values higher than most literature data. The LIS results are still inferior to the outstanding ones obtained in this work via the well-consolidated SC, underlining how promising the more advanced LIS technology, paired with oven sintering, could be in the ISRU framework.

1. Introduction

In the past ten years, most of the space agencies and companies around the world have discussed programs that involve the exploration of the planet Mars [1–5]. Prolonged human presence on the Red Planet is expected to extensively rely on the so-called In-Situ Resource Utilization (IRSU) approach, which is based on the principle of maximizing the in-situ utilization of available space resources to obtain products that significantly reduce the mass, cost, and risk of near-term and long-term space exploration, allowing to cut payload costs especially associated with longer-term missions [6].

Construction materials are expected to be among the most needed resources for the development of permanent bases on Mars's surface [7], as well as an early concern, given the harsh environmental conditions that include harmful radiation, dust storms and boulder impacts [8–10].

Due to the high availability of rocks and regolith, such materials can be considered an easier solution to address this need. The separation of the different mineral phases would require significantly higher energy

* Corresponding author.
E-mail address: David.Karl@ceramics.tu-berlin.de (D. Karl).

https://doi.org/10.1016/j.ceramint.2026.03.213
Received 31 October 2025; Received in revised form 11 March 2026; Accepted 14 March 2026
Available online 16 March 2026

consumption compared to their direct utilization [10]. However, as Mars is a differentiated terrestrial planet with a complex geological history, mineral deposits could be exploited in order to enrich the proposed construction materials of particular phases, with the ultimate aim of tailoring the regolith properties and facilitating processability [11]. In this regard, numerous clay deposits have been detected on the surface of Mars [12].

Given its high versatility, clay shaping is expected to have extraordinary impact as an ISRU technique [13], but water is required for this scope. Numerous pieces of evidence of H_2O presence on planet Mars have been proposed, either as subsurface ice [14], hydrated materials [15], or salt-rich brines [16–18]. The latter two sources of water are usually associated with high concentrations of dissolved salts, that could allow the stability or metastability of brines on the surface of Mars, where pure liquid water is not stable [19].

While most previous clay processing studies were based on the use of pure H_2O [11,13,20], the direct utilization of salt brines for construction materials would eliminate the need for purification processes, thus enhancing the applicability of the proposed technology, especially in the early stages of human presence on Mars.

Given the unavailability of Martian soils and brines for research, which have never been brought to Earth, both regolith and brine simulants are required for Earth-based ISRU studies. In this regard, while several Martian regolith simulants are currently available for researchers [10], limited efforts have been made to simulate Martian saltwater, whose composition is known, based on measurements carried out by the Phoenix lander on Mars [19,21].

A previous study revealed that additive manufacturing (AM) of clay-rich simulants can lead to green bodies with compressive strength similar to general-purpose concrete, albeit with the aid of polymeric binders [13]. If further increases in mechanical performance are needed, consolidation techniques such as sintering could be employed [11]. Additive manufacturing is expected to play an important role in ISRU technologies, as it would enable flexible remote production. Recently, several AM-based approaches have been proposed in this framework. For example, laser fusion of regolith powder beds led to samples with high porosity (>59%) and Vickers hardness of 710 ± 30 HV [8], material extrusion with phosphoric acid (33 wt% non-ISRU-compatible) led to compressive strengths of about 20 MPa [22]. Robocasting resulted in green bodies with compressive strengths of 7.55 ± 1.33 MPa [13]. Layerwise Slurry Deposition (LSD) led to compressive strength of 30.8 ± 2.47 MPa, before sintering [13], and flexural strength of 57.5/53.3 MPa, when sintered in terrestrial/simulated Martian atmosphere [11]. Recently, injection molding was tested to simulate the binder jetting process by using a 6.25% NaCl aqueous solution as a binder, achieving a peak compressive strength of 25.46 MPa after sintering at 1200 °C for 1 h [23].

Among the traditional technologies employed to process ceramic slurries, slip casting (SC), capable of processing a broad range of particle sizes, allows to obtain high powder packing density, up to 60 % of the theoretical density and a low organic content (typically 2 wt%) is generally employed in the process [24]. These features, including the possibility of employing limited or no polymeric additives, make this technology particularly interesting in the ISRU scenario. SC has previously been employed on Martian regolith slurries both for the obtainment of unfired green bodies (compressive strength of 3.34 ± 0.22 MPa, 42.2% porosity) [11] and sintered parts (flexural strength of 51 MPa, 28.23% porosity) [20].

Recently, the innovative Laser Induced Slip Casting (LIS) technology, falling in the category of additive manufacturing processes, has been proposed as the evolution of conventional SC, being capable of obtaining voluminous ceramic parts with properties comparable to those of conventionally manufactured ones [25].

LIS technology is based on the selective drying of a slurry using a laser (Fig. 1), with many features resembling the well-established stereolithography [25]. If compared to conventional SC, LIS allows faster generation of parts with random geometries without the need for gypsum molds [26] and with the automation advancements associated with AM processes [25]. In the framework of ISRU studies, LIS technology could provide control of the density of the printed part, from low values (e.g., compatible for thermal insulation applications), to very high compaction levels [27]. Moreover, this technology could enable fast production of regolith-based parts, as higher build rates, with respect to other ceramic AM forming techniques, have been reported (up to 60 mm/h throughput versus 5–10 mm/h) [27]. LIS is therefore compatible with remote automated production, which could anticipate and prepare a human mission on Mars, an aspect that is often identified among the main advantages of AM within the ISRU context [10].

LIS technology is evaluated for the first time in the present work as a possible ISRU additive manufacturing technology for the obtainment of sintered parts with compressive strength equal to, or higher than, general-purpose concrete (i.e., 20-40 MPa). Samples obtained with

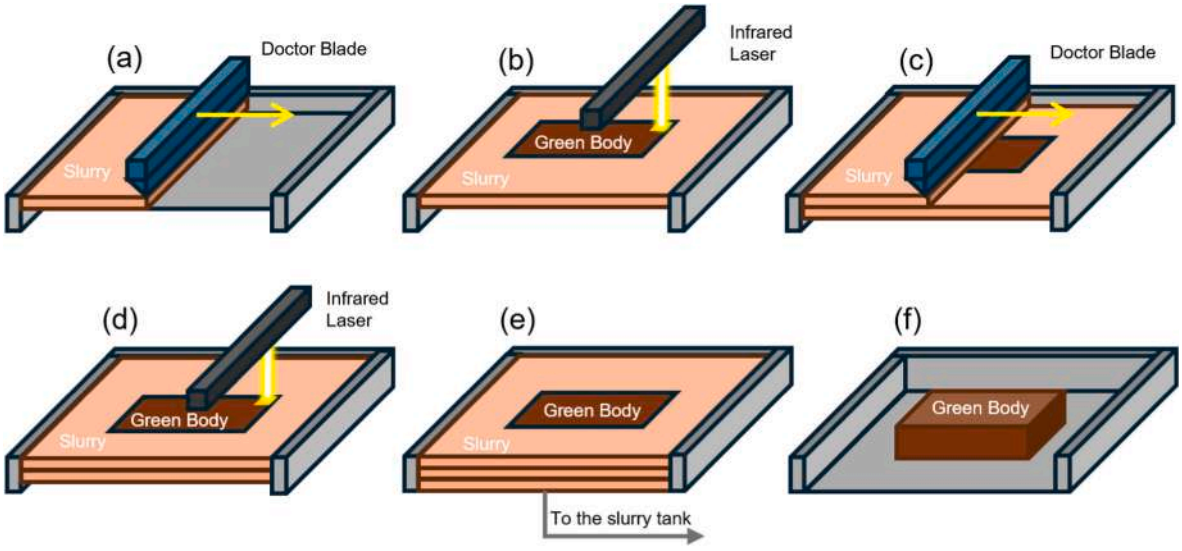

Fig. 1. Illustration of the LIS process, a) The first layer of slurry is deposited in the build platform by the doctor blade. b) The laser locally dries the slurry, producing the first layer of the green body. c) A new layer of slurry is deposited. d) The laser locally dries the second layer of slurry. e) The excess slurry is drained. f) The printed green body remains.

conventional SC have been produced for the sake of comparison. No polymeric dispersant or binder is employed and, to maximize applicability as well as ISRU compliance of the proposed technology, a Martian Saltwater Simulant [21], instead of deionized water, is used as a dispersion medium.

Relative density, linear sintering shrinkage, composition, microstructure and compressive strength of the obtained green bodies are evaluated. Sintering experiments are carried out in both terrestrial and simulated Martian atmosphere conditions [11]. Relative density, water absorption (as frost-resistant ceramics are expected to have water absorption < 3-5% [11,28]), composition, microstructure, magnetic properties, thermal conductivity in the Martian temperature range, and finally compressive strength of sintered parts are examined. Obtained results are compared with literature data.

2. Experimental materials and methods

2.1. Regolith and saltwater simulants

The third-generation simulants, Mars Global Simulant (MGS-1) and (MGS-1C), consist of blends of minerals of appropriate composition and physical properties that closely mimic the Martian soil [10,29]. Their chemical and mineralogical compositions are reported in Tables 1 and 2, respectively[13,30,31].

The main difference between MGS-1 and MGS-1C simulants is the presence of phyllosilicate in the latter. MGS-1C is specifically crafted to simulate a clay-rich Martian terrain, albeit using montmorillonite (Na smectite) instead of nontronite and saponite (Fe/Mg smectites), which have been reported to dominate on the Martian crust but are rare on Earth [13]. Clay minerals allow for the wet processing of Martian regolith without the need for any additional binder or plasticizer, as was reported in previous literature findings [13]. However, high amounts of clay can be detrimental, particularly due to problems associated with shrinkage and cracking phenomena occurring during drying and sintering. The scenario usually proposed to mitigate this issue is to properly temper a high clay content terrain, possibly sourced from phyllosilicate deposits on Mars, with a generic soil with composition close to the Martian average [13]. MGS-1C (40% montmorillonite, see Table 2) and MGS-1 are good candidates to mimic the former and the latter, respectively. In this work, MGS-1C was added to MGS-1 according to different extents, varying from 1:32 to 1:4. The calculated oxide constituents and mineral composition of the 1:16 mixture (MGS-1/16) have been reported in Tables 1 and 2, respectively.

Given the rather coarse dimensions of the as-received simulants, a preliminary dry milling step of the two materials was performed separately. For such a procedure, a steel milling vessel in a vibratory disc mill TS250 (Siebtechnik GmbH, Germany) was employed for treatments of 8 min duration. The Martian saltwater simulant (MSW) was prepared according to the Mars "dirty" water recipe based on the chemical compounds detected by the Phoenix lander [21], as reported in Table 3. Double-deionized water (DDW) was used as a solvent.

Table 1
Oxide constituents (wt.%) of MGS-1 and MGS-1C simulants and the MGS-1/16 mixture employed in this work. Producer values, as well as values obtained via XRF on the same batches used in this work, have been taken from Karl et al. 2020a and references therein [13]. The calculated MGS-1/16 mixture values refer to the latter.

Oxide	MGS-1 (Producer data)	MGS-1 (measured)	MGS-1C (Producer data)	MGS-1C (Measured)	MGS-1/16 mixture (calculated)
SiO_2	45.57	44.36	53.16	51.15	44.78
Al_2O_3	9.43	12.71	16.89	13.98	12.79
FeO_T	16.85	16.85	8.24	10.86	16.48
MnO	0.1	0.1	0.04	0.05	0.10
MgO	16.5	13.84	12.57	6.84	13.40
CaO	4.03	7.36	2.02	3.48	7.12
Na_2O	3.66	1.65	1.91	2.24	1.69
K_2O	0.43	0.46	0.47	0.54	0.47
TiO_2	0.3	0.39	0.21	0.28	0.38
P_2O_5	0.37	0.11	0.35	0.09	0.11
Cr_2O_3	0.12	0.13	0.02	0.04	0.12
SO_3	2.63	1.73	1.16	1.05	1.69

Table 2
Phase composition (wt.%) of MGS-1 and MGS-1C simulants and the MGS-1/16 mixture employed in this work (n.r.: not reported).

Mineralogical Phase	MGS-1 [30]	MGS-1C [31]	MGS-1/16 mixture (Calculated)
Glass-rich basalt	22.9	13.7	22.3
Plagioclase	27.1 (Anorthosite)	16.4 (Anorthosite)	26.4 (Anorthosite)
Pyroxene	20.3	12.2	19.8
Olivine	13.7	8.2	13.4
Mg-sulfate	4.0	2.4	3.9
Anhydrite	1.7	1.0	1.7
Ferrihydrite	3.5	2.1	3.4
Spinel	1.9 (Magnetite)	1.1 (Magnetite)	1.9 (Magnetite)
Hematite	0.5	0.3	0.5
Fe-carbonate	1.4	0.8	1.4
Hydrated silica	3.0	1.8	2.9
Phyllosilicates	n.r.	40.0 (Montmorillonite)	2.5 (Montmorillonite)

2.2. Wet processing

2.2.1. Slurry preparation

After the milling step, powders were mixed according to different MGS-1C to MGS-1 ratios to obtain blends with clay content ranging from 1% to 10 wt%. MSW was added to the desired extent. A wet milling step was then performed to guarantee a proper dispersion of the regoliths in the saltwater simulant. A 1h treatment on a roller bank (ROBO, Alpine, Germany) set at 150 rpm was performed using 8 mm diameter (30% of slurry weight) and 3 mm diameter (10% of slurry weight) zirconia balls as milling media.

2.2.2. Slurry characterization

Prior to printing, a rheological characterization was performed by tuning clay content in solids and solid loading to find an optimum that guaranteed the best slurry processability.

Viscosity of the slurries was measured by means of a Physica MCR301 rheometer (Anton Paar, Austria). The shear rate was systematically varied using a linear ramp from 5 to 100 1/s over a duration of 145 s, and then kept constant at 100 1/s for a duration of 10 s before being linearly ramped back down to 5 1/s.

Other than viscosity, shear stress was investigated as a function of shear rate.

Slurries produced according to different MGS-1C to MGS-1 ratios and 50 wt% solid loading were then preliminary slip cast with a conical mold and characterized in terms of the extent of cracks formed during printing and subsequent drying.

Particle size distribution of the solids dispersed in the slurry was determined using an LS13320 laser diffraction size analyzer (Beckman Coulter, USA). Each measurement was repeated three times.

Given the use of a CO_2 infrared laser to dry the slurry during LIS printing, the optimized composition was characterized in terms of infrared radiation absorbance, taking inspiration from the work of Goulas et al. [8]. To this aim, spectra were obtained by means of a Fourier transform infrared (FTIR) Vertex 70 (Bruker, Germany) spectrophotometer in the wavelength range 4-20 μm. For the sake of comparison, powders mixed according to the optimized clay content were also characterized.

Table 3
Mars saltwater simulant (MSW) composition (1 L solution) taken from Linne et al., 2019 [21].

Formula	Compound	Quantity (g)	Supplier	Product Code
H_2O	Double deionized water	1000	-	-
$CaCO_3$	Calcium Carbonate	1.6	Riedel-de Haen AG Seelze-Hannover	12003
$MgCO_3$	Magnesium Carbonate	0.8	Roth	3530.2
$MgSO_4$ *$7H_2O$	Magnesium Sulfate Heptahydrate	1.2	Merck	5886
KCl	Potassium Chloride	0.032	Roth	6781.1
$NaHCO_3$	Sodium Bicarbonate	0.14	Honeywell Fluka	31437
$Ca(ClO_4)_2$ *$4H_2O$	Calcium Perchlorate Tetrahydrate	0.46	ThermoFisher Scientific	39063
$Mg(ClO_4)_2$ *$6H_2O$	Magnesium Perchlorate Hexahydrate	0.332	Aldrich	309303

2.2.3. LIS printing

LIS printing was performed using a CeraMax Vario V900 LIS machine (Lithoz, Austria).

The CeraMax Vario V900, depicted in Fig. 2a, is equipped with a 120 W CO_2-Laser that has a focused spot with a diameter of ~0.5 mm. The slurry is stored in a reservoir from which it is pumped and spread out by a doctor blade, which deposits it on a build plate (Fig. 2b) that is lowered into the vat for every new layer. During printing, the infrared CO_2 laser progressively dries the slurry according to customizable parameters, as described in the Supplementary Material.

Fig. 2c and d shows examples of alumina parts printed through optimized LIS parameters.

In this study, two configurations, namely A and B, respectively, are tested (Table 4). With respect to the B one, configuration A is an enhanced drying program which aims to maximize water removal from each printed layer, thanks to an increased Wattage and Number of Hatches. To maximize the output of the printing sessions, rather simple blocks of dimensions 80x80x5 mm are printed with the LIS machine, and smaller square-section green bodies with a 2:1 aspect ratio (dimensions about 15x5x6 mm) are cut from them.

2.2.4. Slip casting

For the sake of comparison, the same optimized slurry composition employed for LIS printing was used to obtain, via slip casting, cylindrical samples of aspect ratio >2:1 (dimensions about 15 mm height x 6 mm diameter). To do so, polymeric cylindrical molds, treated with a mold release spray, were employed on top of a gypsum plate.

Table 4
Investigated parameters for the LIS process. Values reported in italics identify a parameter that was varied and optimized for the obtainment of the LIS printed part.

Parameter	Config. A	Config. B
Laser Speed	7 m/s	7 m/s
Wattage	*30 W*	*22 W*
Line Spacing	0.025 mm	0.025 mm
Number of Hatches	*30*	*22*
Rotation Between Hatches	90°	90°
Line Scheme	Snake	Snake
Layer Height	0.25 mm	0.25 mm
Dimensions of the Printed Part	80x80x5 mm	80x80x5 mm

2.3. Thermal treatments

2.3.1. Preliminary Thermogravimetric analyses

Thermogravimetric analyses (TGA) were performed to evaluate the degassing behavior in oxidizing and inert atmospheres of LIS-printed green bodies undergoing sintering. The experiments were performed

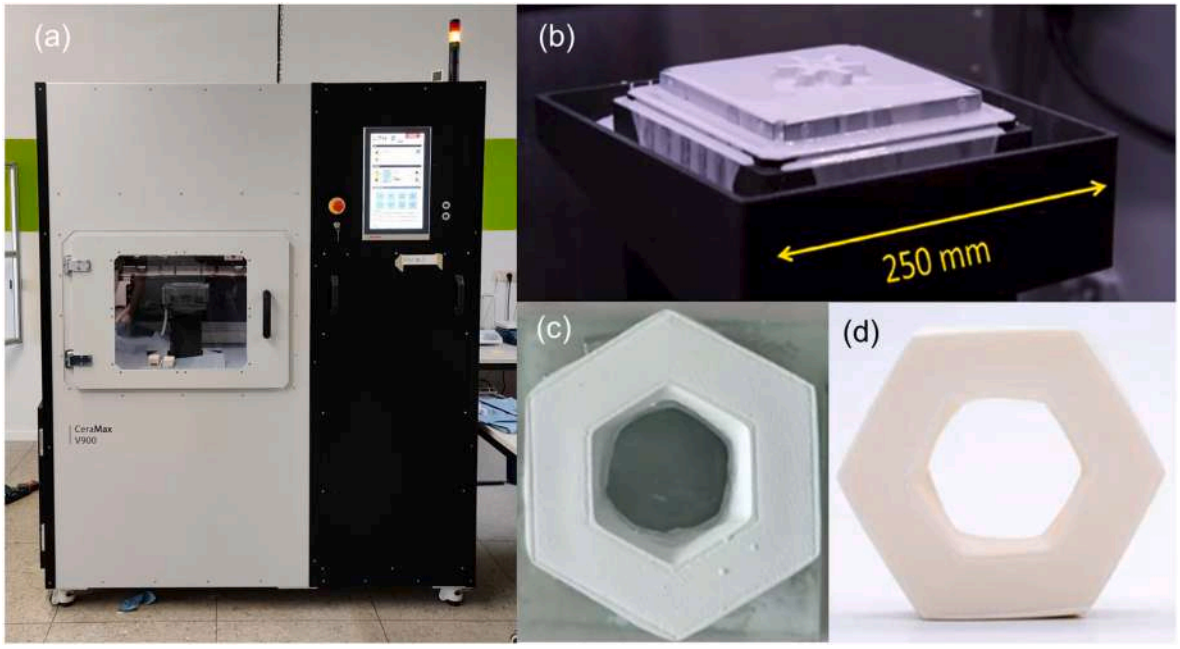

Fig. 2. (a) The CeraMax Vario V900 machine for Laser Induced Slip-Casting employed in this work. (b) Details of the build platform, (c) and (d) examples LIS printed alumina parts.

with a simultaneous DTA-TGA STA 409 PC Instrument (Netzsch, Germany) coupled with an OmniStar mass spectrometer (Pfeiffer Vacuum, Germany). The weight loss and evolved gas were tracked in the RT-1200 °C interval, with a heating rate of 10 K/min.

To evaluate the effect of the salts on the thermal stability of the printed part, tests experiments were conducted in an air atmosphere for the MSW green body printed via LIS and a special LIS-printed green body was obtained with DDW. Additionally, inert conditions experiments were conducted in the N_2 atmosphere for MSW LIS printed samples. Each experiment was reproduced at least twice.

2.3.2. Sintering

A custom-built Al_2O_3 tube furnace inside an HT 1600 (LECO Instruments GmbH, Germany) was used to heat samples from room temperature to a dwelling value in the range of 1150°C-1210 °C with 3 h dwelling time and 1.7 K/min heating/cooling rate. Two-step treatments were performed by augmenting with the same heating rate the lower dwell temperature up to the upper value, which was kept for an additional 1 h dwelling time. Experiments were conducted both in oxidizing (air) and simulated Martian conditions (925 Pa CO_2). Further details on simulated Martian atmosphere sintering can be found elsewhere [11]. A minimum of three samples (SC and LIS) were placed inside the sintering area to evaluate experimental deviations.

2.4. Characterizations of the dense samples

Sintered samples were characterized in terms of the corresponding linear shrinkage and relative density. The latter was evaluated by Archimedes' method using acetone as a soaking medium (as suggested by Sizemore et al. [32]) and an MC1 Analytic AC210P (Sartorius, Germany) analytical balance. Relative densities were then calculated by considering, as reference values, the true densities evaluated on crushed LIS green body by an Ultrapyc 1200e helium pycnometer (Quantachrome Instruments, USA). Water adsorption experiments were conducted by submerging the samples in double-deionized water for 10 min and recording the weight before and after the experiments. Phase transitions occurring after the thermal treatments were evaluated by means of ex-situ X-ray Powder Diffraction (XRD) analysis on pulverized sintered samples. A D8 (Bruker, Germany) diffractometer was used (Bragg--Brentano geometry), equipped with a copper anode (Cu Kα radiation $\lambda = 1.5418$ nm) working at 40 kV and 40 mA. The analysis was performed in the range $2\theta = 10°$- 130°, with a step size of 0.05° and 10 s for each step. The attribution of the mineralogical phases was performed with EVA software (Bruker, Germany) with a Search and Match approach, using the COD (Crystallography Open Database) as a reference database [33]. Sample microstructure was investigated prior to and after sintering via high-resolution scanning electron microscopy (SEM, Quanta FEG 400, FEI Company, USA). To estimate the total porosity level and average pore size (equivalent circular diameter and Feret diameter), SEM micrographs representing different areas of each sample were analysed using ImageJ software (National Institute of Health, USA) [34].

Compressive strength was evaluated on 10 LIS and 10 SC samples produced at the two optimized conditions for oxidizing and reducing atmospheres, using a Zwick RetroLine (Zwick/Roell, Germany) machine.

Magnetization measurements on 7 selected samples were performed using the Vibrating Sample Magnetometer option on a Physical Properties Measurement System (PPMS, Quantum Design). The material (15 – 25 mg) was filled into plastic capsules and mounted to brass sample holders. Magnetic hysteresis curves were taken at 300 K in an applied magnetic field up to ±1 T. Heat conductivity between 100 K and 300 K was measured on selected samples using the Thermal Transport Option on the PPMS.

3. Results and discussion

3.1. Compositional optimization of the slurry

Rheologic experiments, as reported in Fig. 3, show that the higher the water content in the slurry (lower solid loading), the lower the viscosity. With decreasing viscosity while keeping almost constant shear stress over the shear rate, the examined slurries show shear-thinning behavior. As also shown in Fig. 3, the viscosity of the reference Al_2O_3 slurry, which was provided by the company QEP3D as standard for LIS printing, is almost constant over the shear rate, linearly increasing with the shear stress. This slurry shows less shear thinning and behaves as a Newtonian fluid. While the viscosity of the slurry with 45 wt% water is the closest to the Al_2O_3 reference at a shear rate of about 20 1/s, it gets considerably lower at higher shear rates. Overall, the most similar slurry to the reference one, particularly for high shear rates, is that with 50 wt % water. This is important for the LIS process, as the material will experience similar shear rates while being pumped through the tubes. Analogous results have been obtained with the 50 wt% saltwater slurry (50 wt% solid loading), so that such composition was used in all subsequent experiments.

Preliminary slip casting of slurries obtained starting from MGS-1 and MGS-1C simulants mixtures in the range from 1:32 (1 wt% clay) to 1:4 (25 wt% clay) confirmed that the higher the clay content, the more extensive the cracks formed after drying. To keep a good compromise between the processability of the slurry and cracking phenomenon, the 2.5 wt% (MGS-1/16) clay composition was selected and used for all experiments.

As reported in Supplementary Figure S2, IR spectra of the MGS-1/16 powders show a relatively high absorbance at wavelengths of 10 μm, suggesting that the CO_2 laser is well suited to dry the slurry efficiently.

According to particle size analysis results reported in Table S1, the combined effect of dry and wet milling leads to a slurry characterized by small, dispersed particles, showing a D_{90} parameter of 8.28 μm.

3.2. Additive manufacturing

The saltwater-based slurry prepared according to the optimized solid loading (50 wt%) and mixture of MGS-1 and MGS-1C simulants (MGS-1/16 powders) was printed according to A and B configurations reported in

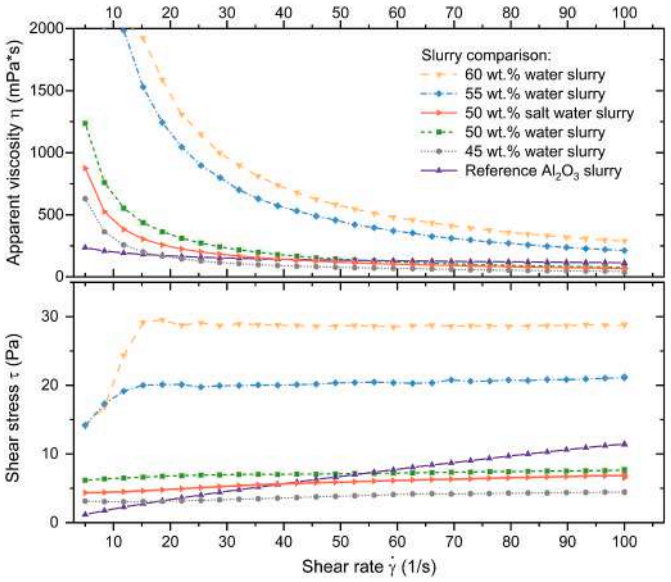

Fig. 3. Viscosity and shear rate over shear stress for different slurries: comparison of 60-45 wt% water (dashed lines), 50 wt% saltwater (red solid line line) content and Al_2O_3 reference slurry (violet solid line).

Table 4.

While B succeeded in printing the 80x80x5 mm block (Fig. 4b), when printing with configuration A, cracks appeared already during the LIS process, as reported in Fig. 4a. This difference is ascribable to the harsher drying in the latter configuration, where both laser Wattage and Number of Hatches parameters were higher. This likely resulted in humidity gradients across the printed part, causing cracks and exfoliation.

This outcome underlines the importance of the tunability of LIS parameters, if compared to traditional slip casting, when it comes to controlled drying. By appropriately tuning two of the machine parameters, it was possible to obtain 80x80x5 mm blocks, which were then cut into smaller square-section green bodies dimensions about 15x5x6 mm, used for subsequent sintering and characterization.

Cylinders of about 15 mm in height and 6 mm in diameter were obtained through slip casting (Section 2.2.4). Their sintering and characterization results were used as a comparison for those obtained for the LIS samples.

LIS printed parts showed an average density of 1.63 ± 0.07 g/cm^3, while a higher value of 1.83 ± 0.03 g/cm^3 corresponded to SC samples. If compared to the pycnometric density of 3.03 ± 0.01 g/cm^3, measured on the dried starting slurry, the relative densities for the green bodies are about 53.8% and 60.4% for the LIS and SC samples, respectively.

Such differences could be likely ascribable to the diverse drying conditions encountered by the same material. In the LIS process, the new slurry is progressively added on top of each dried layer during printing, causing water reabsorption that could determine a resulting higher water content at the end of the process, if compared to SC. This water content is then eliminated through the final drying step in a controlled atmosphere. However, a higher porosity is retained.

Such findings are confirmed by the LIS and SC green bodies micrographs reported in Fig. 5a–d. The printed parts consist of agglomerated particles. The effect of the printing process can be clearly observed in unpolished LIS samples (Fig. 5b), where ~250 μm wide layers are present, consistently with the layer height parameter chosen during printing (see Table 4). Conversely, such a structure is absent in SC specimens (Fig. 5a). Clearer insights can come from micrographs of resin-embedded and polished samples, for which higher porosity levels, estimated and reported in Supplementary Table S2, can be observed in the case of LIS (Fig. 5d). Even if the obtained values are slightly overestimated (porosities of ~57 and ~48 % for LIS and SC, respectively), most probably due to epoxy infiltration, a clear difference can be observed between the two printed parts.

3.3. Thermogravimetric analyses

Thermal stability of the obtained LIS green bodies was evaluated in different atmospheres. Fig. 6a shows the weight loss and developed gas occurring in air for LIS-printed green bodies according to configuration B (see Table 4) in the case of MSW-based and DDW-based slurries. This comparison aims to highlight possible differences deriving from the salts added during the preparation of the liquid dispersion medium MSW (Table 3).

From Fig. 6a, it can be observed how both the MSW and DDW-based green bodies show a rather similar behavior, with progressive mass decrease when exposed to rising temperatures, and a final loss of about 4.9% at 1200 °C. This phenomenon, other than to water evaporation, can be attributable to the thermal decomposition of carbonates and sulfates. The latter takes place both in MSW and DDW samples, indicating that its origin lies not only in the added salts (which account for no more than 0.5 wt% in the case of MSW-based green bodies) but also in the raw powders, particularly rich in $MgSO_4$ and $FeCO_3$ (see Table 2). Looking in detail at the spectra of the gases developed during TG analyses, two peaks in the CO_2 signal (blue lines) are detected at about 400 °C and 600 °C for both green bodies. These signals are attributable to carbonates, whose decomposition is expected to produce CO_2. Indeed, the same phenomena were detected for natural phases in the 350°C-450 °C range for the case of siderite ($FeCO_3$) [35], 450-700 °C for magnesite ($MgCO_3$) [36] and 600-800 °C for pure calcite ($CaCO_3$) [37], all species either present in the pristine simulants (Table 2), or added during the preparation of MSW (Table 3).

Looking at the SO_2 spectra (green lines), a significant increase in concentration can be observed for temperatures higher than 800 °C, in agreement with the decomposition of magnesium sulfate usually observed in the range 800-1100 °C [38]. The consequent drop in the weight loss curve can be related to such a phenomenon.

Fig. 6b shows that a limited impact is generated when thermal treatment in inert conditions is conducted, such as in N_2 atmosphere. Indeed, a slight (1.4%) decrease in mass loss is correspondingly observable, with a final value at 1200 °C equal to 3.5%. The most significant difference is the anticipated onset of the SO_2 degassing, which could be related to the occurrence of $MgSO_4$ decomposition at lower temperature levels, as also observed when operating in reducing conditions [38,39]. The latter ones are likely established in this work due to interactions with other reducing species in the tested powders, which are allowed by the absence of free oxygen in the flowing gas.

3.4. Sintering conditions optimization

Fig. 7 evidences the recorded results in terms of relative density, water adsorption and linear sintering shrinkage recorded for the LIS and SC printed green bodies sintered under oxidizing conditions (air atmosphere). Relative density increases when the dwelling temperature of

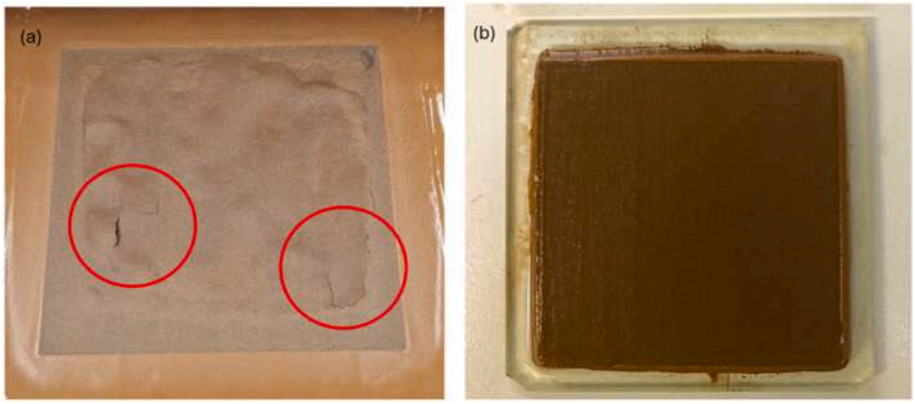

Fig. 4. LIS parts (80x80x5 mm) printed according to configuration A (a) and configuration B (b), starting from MSW slurry. The part printed according to configuration A was photographed while still in the build platform, when cracks (highlighted with red circles) started to appear due to the more severe drying routine employed.

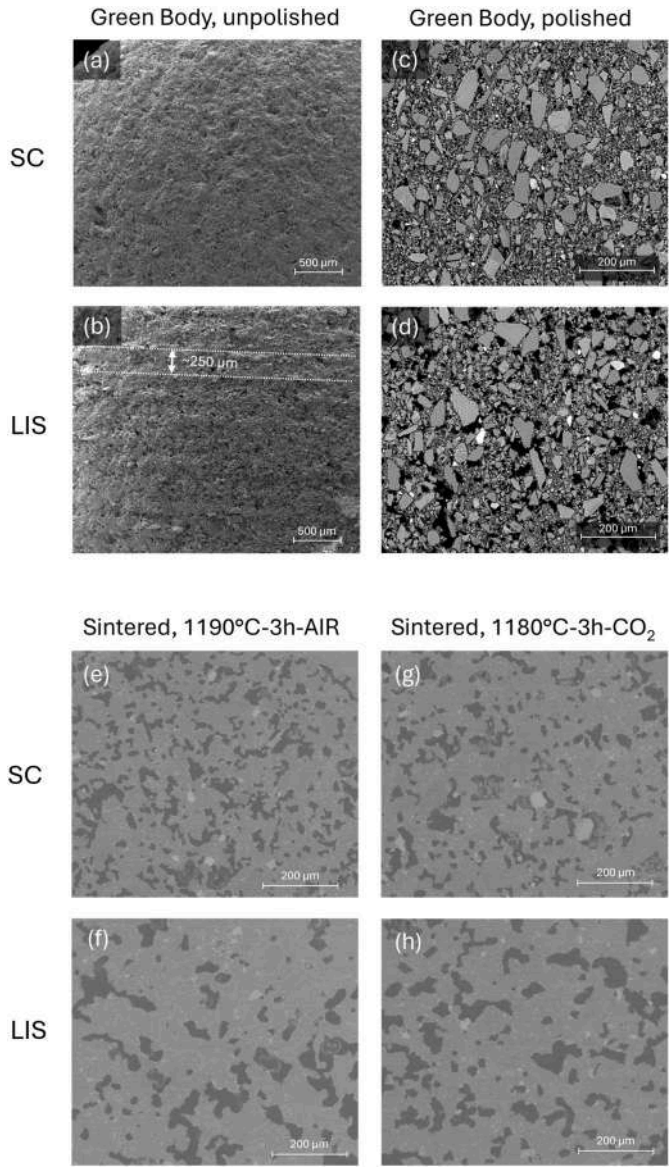

Fig. 5. SEM micrographies of unpolished green bodies (a: LIS, b: SC); polished green bodies (c: SC, d: LIS); samples sintered at 1190°C-3h in air (e: SC, f: LIS); and at the 1180°C-3h condition in simulated Martian atmosphere (g: SC, h: LIS), evidencing the different morphology before and after sintering and between LIS and SC specimens. The represented samples are those characterized by their compressive strength.

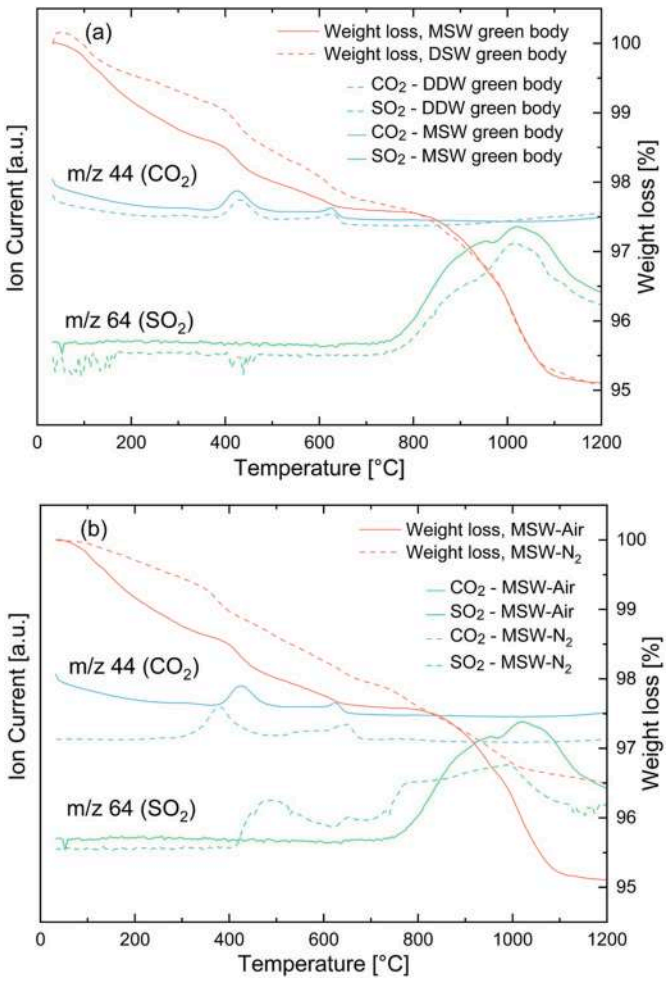

Fig. 6. Weight loss and evolved gases during the TG analyses in air. (a) Comparison between LIS-printed green bodies prepared with DDW (dashed lines) and MSW (solid lines). (b) Comparison of TG analyses in air (solid lines) and N_2 (dashed lines) for the case of LIS-printed green bodies prepared with MSW. CO_2 (blue lines, molar mass of 44 g/mol) and SO_2 gases (green lines, molar mass of 64 g/mol) have been considered for the mass spectroscopy measurements.

the sintering process is gradually raised (Fig. 7a). It can be noted that the relative density gap observed for LIS and SC green bodies is maintained for all sintering conditions up to T_D = 1190 °C, until an asymptotical level of about 85-86% is achieved at $T_D \geq 1200$ °C for both samples. As reported in Fig. 7b, specimens obtained at $T_D \geq 1200$ °C also show high linear sintering shrinkages (>9%) and very low water absorption (<1%), suggesting that the sintering phenomenon is causing significant shape changes and porosity reduction. To calculate the relative densities, the theoretical value of 3.03 g/cm^3, obtained for the crushed LIS green bodies, was used. Further pycnometer analyses on the crushed sintered samples suggest that only marginal variations in theoretical densities occur during sintering, with obtained values ranging from 3.03 to 3.05 g/cm^3.

The samples obtained at $T_D \geq 1200$ °C (Fig. 8) showed significant deformation and onset bloating, as well as severe adhesion to the sintering plate. These aspects are not compatible with the acceptable shape retention goal proposed for this study and have, therefore, been considered unsuitable for further characterization.

The harsher sintering condition that avoids such phenomena, while still guaranteeing acceptable densification levels, is 1190°C-3h. However, water adsorption is still >3% for the case of LIS samples (4.93 ± 2.09%). In Karl et al. [11], adding a second sintering step at a 10 °C higher temperature after the first 3 h dwelling at the original T_D value, resulted in lower water absorption and more prominent linear shrinkage, so that bloating and excessive deformation due to the limited time at the higher temperature level are both prevented. In this study, operating with a two-step 1190°C-3h + 1200°C-1h sintering routine succeeded in obtaining samples with low water absorption (0.88 ± 0.16% LIS, 0.54 ± 0.13% SC), but the same problems observed with one-step sintering at $T_D \geq 1200$ °C were also encountered. This different behavior, if compared to the results reported in Karl et al. [11], could be ascribable to the lower clay content in the green bodies (5 vs 2.5 wt% in this study) and the milder T_D employed in the previous work (1145 °C), all aspects capable of allowing a higher processability and finer tunability of the sintering conditions.

Given the negative outcome of the two-step test, the 1190°C-3h sintering condition was considered as the optimal for producing samples to be tested for compressive strength and further characterizations. The relative densities achieved in the case of LIS and SC samples are 77.82 ±

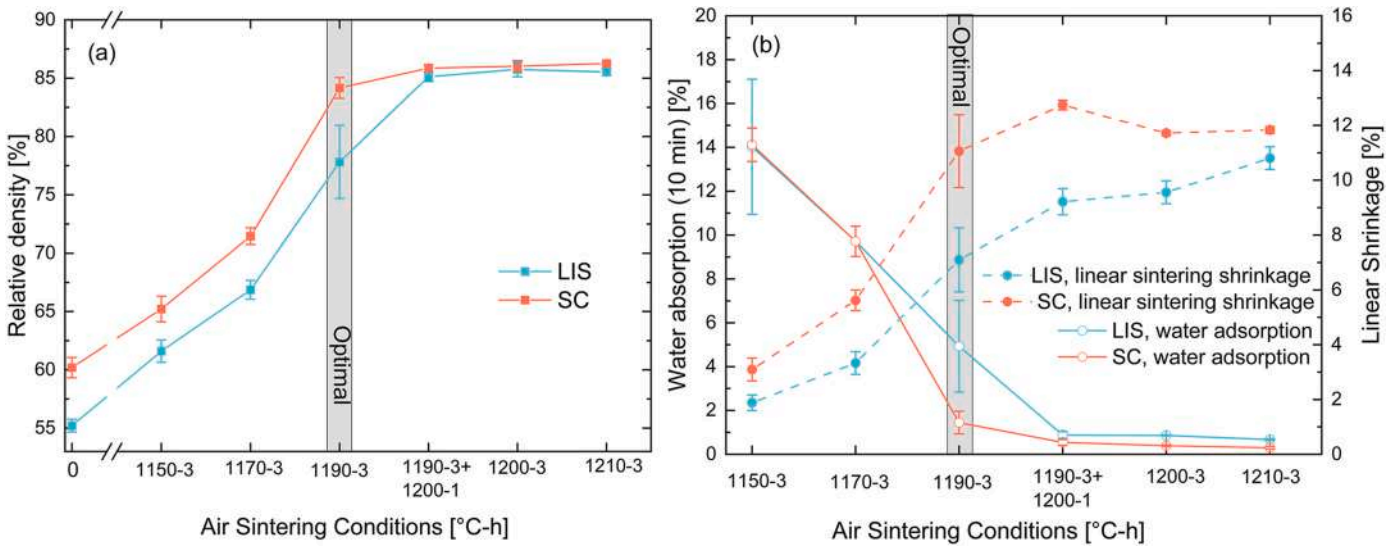

Fig. 7. Sintering test results in terms of (a) relative density and (b) 10 min of water adsorption and linear sintering shrinkage in an air atmosphere. The grey box evidences the optimal samples. The sintering conditions are represented in terms of maximum temperature [°C]-sintering time [h]. Relative density was calculated as the ratio of measured and pycnometric density, water absorption as the relative difference between the weight of the sample after 10 min immersion in deionized water and its dry weight, and linear shrinkage as the relative difference of the sample length before and after sintering.

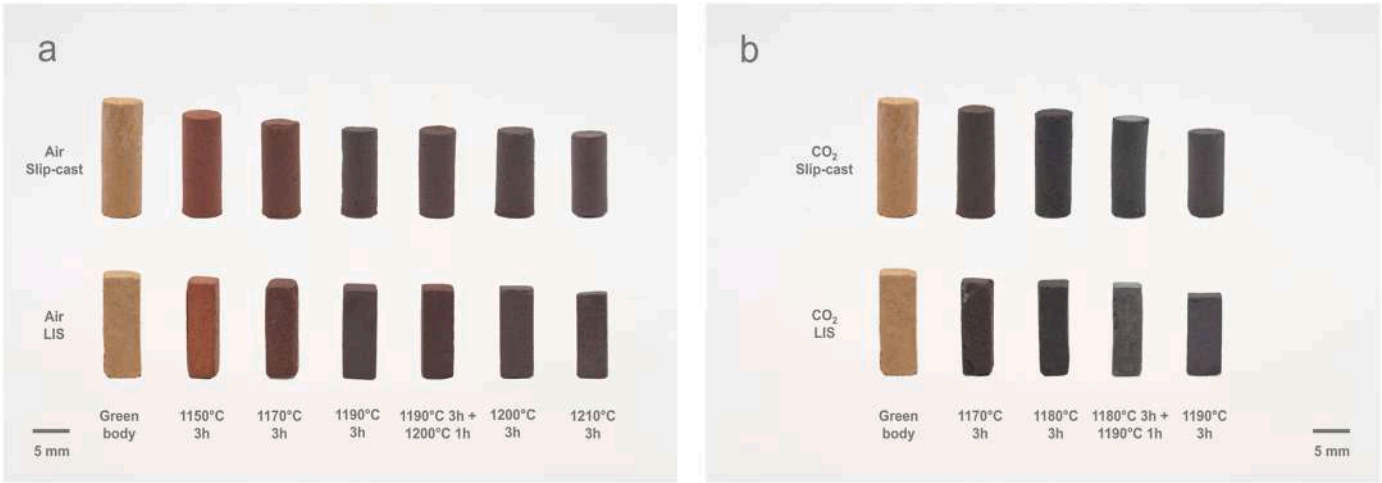

Fig. 8. Samples sintered under different conditions in (a) air and (b) simulated Martian atmosphere. The first row of samples refers to SC, while the second row refers to LIS ones. Sintering conditions have been reported at the bottom of the pictures. The images were produced by combining photos of individual samples (due to different perspectives in these photos and slightly varying green body sizes, the heights were adapted to match the observed linear sintering shrinkages).

3.14% and 84.16 ± 0.89%, respectively.

When operating under simulated Martian conditions (i.e., 925 Pa CO_2), similar trends in relative density, water absorption and linear sintering shrinkage can be observed (Fig. 9).

In this case, and in agreement with previous findings [11], operating under a simulated Martian atmosphere causes a slight shift of the sintering window towards milder conditions. Working at 1190°C-3h under CO_2, bloating, significant deformation and adhesion occur. Thermal treating the samples at 1170 °C causes a marked reduction in terms of relative density, linear shrinkage and an abrupt increase of water absorption. On the other hand, relatively high densification levels both for the case of LIS (relative density of 82.08 ± 3.26%) and SC samples (relative density of 82.71 ± 1.62%) are obtained when operating at the middle point of 1180 °C for 3 h. The two-step sintering schedule 1180°C-3h + 1190°C-1h was tested to improve further the water absorption parameter, which is 4.10 ± 1.97% at 1180°C-3h in the case of LIS samples. This strategy is successful in obtaining the desired water absorption level while also increasing relative density for both LIS and SC specimens. However, as recorded for the air atmosphere tests, it is sufficient to generate pronounced deformation and adhesion to the sintering plate. For this reason, the 1180°C-3h condition was considered as the optimal for producing samples to be futher characterized.

Similar relative densities were found between LIS and SC samples for the case of CO_2 sintering (Fig. 9a), with respect to the air results (Fig. 7a). This difference can be ascribable to the fact that the samples tested under CO_2 atmosphere earlier approached high densification levels. Such features might be linked to the evolution of the Magnetite phase in the samples, as described below. Further considerations on the sintering behavior of such regolith-like materials can be found in previous works, both for the case of sintering in air [11,40] and simulated Martian atmosphere [11]. In particular, Gupta et al. [40] proposed a sintering mechanism applicable to regolith simulants that indicates how volume diffusion is the main phenomenon affecting such process.

Details on the microstructure of the LIS and SC samples prior to and after sintering are depicted in Fig. 5. Sintering of the unconsolidated green bodies (Fig. 5a–d) allows for the obtainment of more uniform

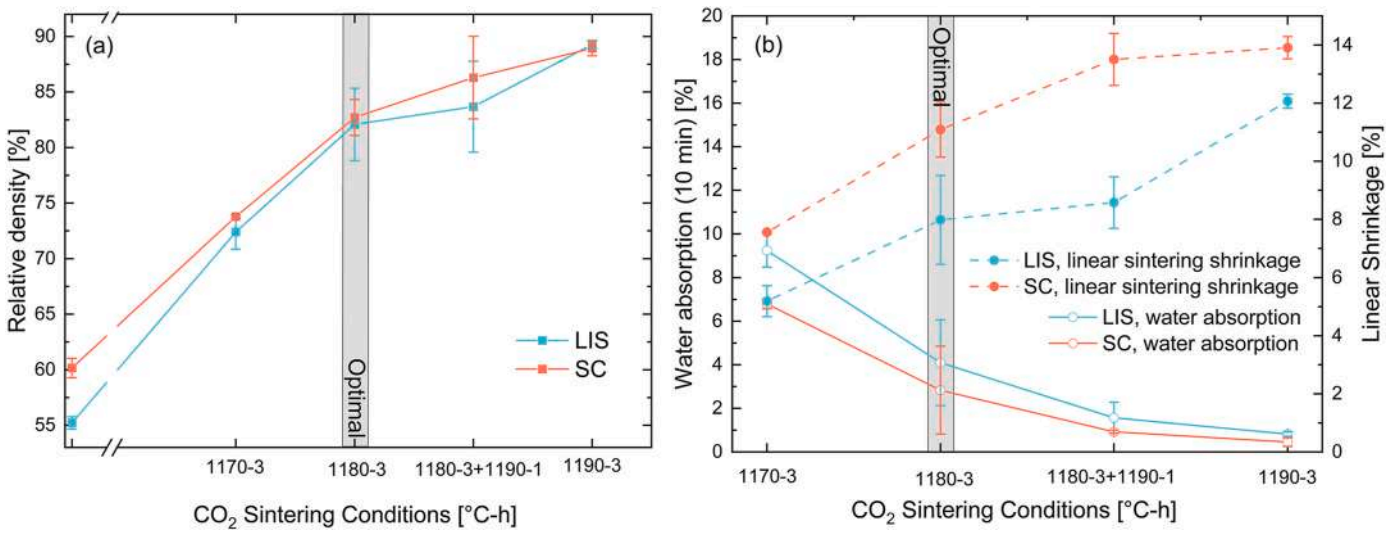

Fig. 9. Sintering test results in terms of (a) relative density and (b) 10 min of water absorption and linear sintering shrinkage in the simulated Martian atmosphere. The grey box evidences the optimal samples. The sintering conditions are represented in terms of maximum temperature [°C]-sintering time [h]. Relative density was calculated as the ratio of measured and pycnometric density, water absorption as therelative difference between the weight of the sample after 10 min immersion in deionized water and its dry weight, andlinear shrinkage as the relative difference of the sample length before and after sintering.

samples (Fig. 5e–h). No major morphological differences can be detected between samples sintered in air and simulated Martian atmosphere. However, the pores of LIS samples appear larger than those present in SC ones. Supplementary Table S2 reports that the estimated porosity levels of the four sintered specimen classes are rather consistent with density data, between 21.6 and 23.4%. Porosity degree is quite similar for all samples, even if slightly higher for the air sintered ones. Much clearer differences can be observed in pore morphology (Fig. 5): LIS samples display fewer but larger pores, while SC specimens present a finer distribution, as testified by the related data reported in Supplementary Table S2. The layers observed in LIS green bodies cannot be distinguished anymore after sintering, most probably masked during polishing and by the presence of significant porosity. Indeed, the layered structure of LIS samples was reported to be retained in the case of highly dense sintered parts [27].

Let us examine the macroscopic features of the samples. From Fig. 8, where photographs of the latter ones are depicted, it can be observed that both LIS and SC samples sintered under an air atmosphere exhibit a gradual color shift from the yellowish-brown of the unsintered sample, to bright red (at 1150°C-3h), finally fading to darker shades of red (until 1210°C-3h). On the contrary, when operating under simulated Martian atmosphere, all samples show a darker color.

This phenomenon is likely an index of undergoing phase transitions in the sintered pieces. To support the latter statement, the obtained samples were subject to compositional analysis.

3.5. Compositional and magnetic characterization

Fig. 10 collects a 2θ = 20°- 60° focus of the XRD spectra of LIS samples sintered in air (a) and CO_2 (b) atmospheres for the case of the optimal conditions 1190°C-3h and 1180°C-3h, respectively, and the milder one 1170°C-3h. The XRD spectrum of the crushed green body has also been reported for the sake of comparison.

To identify the origin of the peaks detected in the latter ones, the XRD patterns of pristine MGS-1 and MGS-1C simulants have been reported in Supplementary Fig. S3. Two dominant phases ascribable to the Plagioclase and Pyroxene groups, a minor Olivine and traces of Siderite ($FeCO_3$) and Epsomite ($MgSO_4$) have been detected. It is worth noticing that a significant amorphous content characterizes these simulants. Basaltic glass, Hydrated silica, and Ferrihydrite all contribute to the amorphous fraction reported by Cannon et al. [29]. It is then possible to state that the detected crystalline phases are in agreement with the compositions reported by the producer (Table 2). Regarding MGS-1C, Montmorillonite, Quartz and Calcite ($CaCO_3$) have also been detected, while the intensity associated with the Epsomite peak is higher than in the case of MGS-1.

In the LIS green body (black line in Fig. 10), Plagioclase, Pyroxene, Olivine and Siderite phases are present, with relevant intensities associated with Epsomite and Calcite phases, mostly deriving from MGS-1C and the salts added by employing the MSW simulant, according to Table 3. The tempering of MGS-1C with MGS-1 caused a reduction in the intensity of peaks associated with Quartz and Montmorillonite phases, which have not been assigned in the green body pattern (black line in Fig. 10).

For the case of the LIS green bodies sintered in air at the intermediate routine of 1170°C-3h, the main observable differences are a rearrangement in the relative intensities of the Plagioclase and Pyroxene-associated peaks as well as the appearance of reflections ascribable to Hematite and Magnetite. This phenomenon is possibly related to a progressive crystallization of the vitreous phases present in the pristine simulants, especially Ferrihydrite and Basaltic glass, as well as to the decomposition of Siderite. Along these rearrangements, it is worth noticing the disappearance of all peaks associated with carbonates (Calcite and Siderite) and sulfates (Epsomite). This corroborates the results obtained by TGA (Fig. 6a), where mass drops associated with CO_2 and SO_2 degassing peaks were evidenced.

The main difference observed in samples processed at 1170°C-3h and 1190°C-3h is the absence of Hematite reflection and the higher intensities associated with Magnetite, as suggested by the zoomed patterns of the 2θ = 30°- 34° region reported in Supplementary Fig. S4a. This agrees with the progressive pigmentation change of sintered samples observable in Fig. 8a. The bright red color of 1170°C-3h samples ascribable to Hematite progressively fades towards darker brown-red starting from 1190°C-3h, suggesting a gradual depletion of such phase.

Fig. 10b indicates that a rather similar behavior with respect to the case of air sintering is encountered when operating in a CO_2 atmosphere. Siderite, Calcite and Epsomite phases are already lost after the treatment at 1170°-3h, for which a general rearrangement in Pyroxene and Plagioclase intensities is also detectable. In this case, no Hematite is formed, while Magnetite peaks are identifiable, as clearly evidenced by Supplementary Fig. S4b.

At the optimized 1180°C-3h condition, a slight increase in the

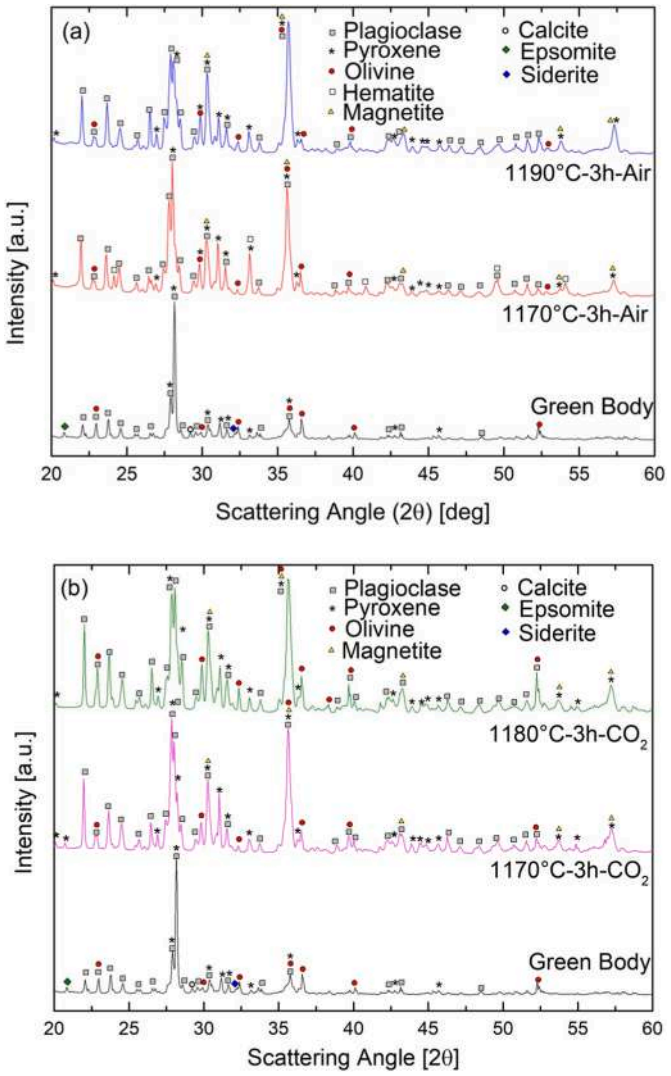

Fig. 10. 2θ = 20°- 60° focus of XRD patterns obtained for the crushed LIS printed green body (black line) and for (a) crushed LIS samples sintered at 1170°C-3h (red line) and at 1190°C-3h (blue line) in air atmosphere and (b) crushed LIS samples sintered at 1170°C-3h (magenta line) and at 1180°C-3h (green line) in simulated Martian atmosphere.

intensity of the Olivine-related peaks was observed, along with a small decrease in Pyroxene-related reflections.

The absence of hematite in the CO_2-sintered samples is consistent with the much darker color of the specimens sintered at 1170°C-3h in the simulated Martian atmosphere, if compared to the ones sintered in air (Fig. 8b).

This feature, which was also observed in the literature [11], suggests that low pressure (925 Pa) CO_2 can generate reducing conditions, that favor the Hematite to Magnetite phase transition [41]. Such a transition was also reported to occurr when exposing these iron oxides to other reducing gases, such as CO or H_2 [41,42].

Due to the scarcity of magnetic data related to Martian regolith simulants [10], the estimate of relative abundance of magnetite in each specimen and a general magnetic characterization are provided. To this, hysteresis curves of the magnetization M were measured at 300 K in an applied magnetic field up to $\mu_0 H = \pm$ 1 T, as shown in Supplementary Figs. S5–S7, while the characteristic parameters extracted from these data are summarized in Fig. 11. All samples exhibit ferro-/ferrimagnetic behavior with values for the saturation magnetization M_s between 1.5 and 3.3 Am^2/kg. Interestingly, all three pristine samples show $M_s \approx 2$ Am^2/kg. These large magnetization values suggest that all samples

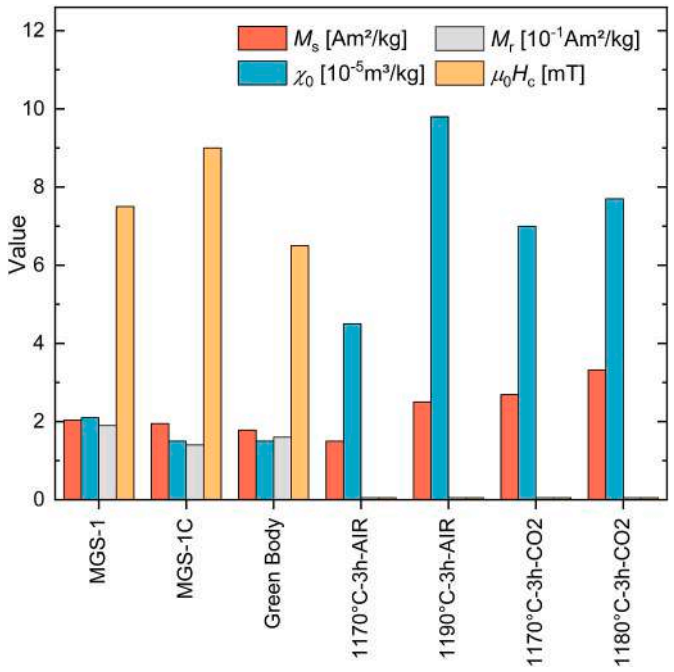

Fig. 11. Magnetic characterization outcomes of the pristine MGS-1 and MGS-1C simulants, the crushed LIS green body, and sintered samples obtained in air for 1170°C-3h, 1190°C-3h and in the simulated Martian atmosphere for 1170°C-3h and 1180°C-3h. Values are extracted from the data presented in Supplementary Figs. S5–S7.

contain a significant amount of Magnetite. The pristine samples are characterized by relatively small values of the initial susceptibility ($X_0 = dM/dH$) at low applied field, while for the sintered ones, this parameter is significantly enhanced. While the pristine materials show significant remnant magnetization (M_r = 0.14-0.19 Am^2/kg) and coercitive field ($\mu_0 H_c$ = 6.5-9 mT), these values appear to be close to zero for all sintered samples. Given the strong dependence of these parameters on crystallite size of Magnetite [43], we associate our observations with the progressive crystallization of the vitreous phases present in the pristine simulants already discussed above, yielding relatively large Magnetite crystallites in the sintered specimens. Notably, M_s is the smallest for the 1170°C-3h air sintered sample, which, according to XRD analysis, contains a significant amount of weakly magnetic Hematite that transforms back to Magnetite for higher sintering temperatures or under CO_2 environment. Thus, the increase of M_s along the row 1170 °C (air) to 1180 °C (CO_2) reflects the increasing fraction of Magnetite in these samples. With the saturation magnetization of Magnetite (92-96 Am^2/kg), we may estimate its fraction in the sintered samples ranging from 1.6% in 1170°C-3h (air) to 3.7% in 1180°C-3h (CO_2). In this regard, it should be noted that the formation of this phase might have a relevant impact on ISRU technologies, as its presence was reported to enhance densification levels and mechanical properties in cement and geopolymers, and have a role in electromagnetic shielding as well as in the removal of metal pollutants [44].

3.6. Thermal conductivity and mechanical characterization

Heat conductivity was measured on the optimal sintered samples produced in air and simulated Martian atmosphere. Values in the range 0.77-0.53 W/mK (air) and 0.80-0.56 W/mK (CO_2), respectively, were recorded in the temperature range 100 K to 300 K (Fig. 12). These values, collected in a temperature range resembling day-night conditions on Mars, are in line with data generally reported for Earth concrete [45].

In Table 5, the compressive strength of LIS and SC green bodies are

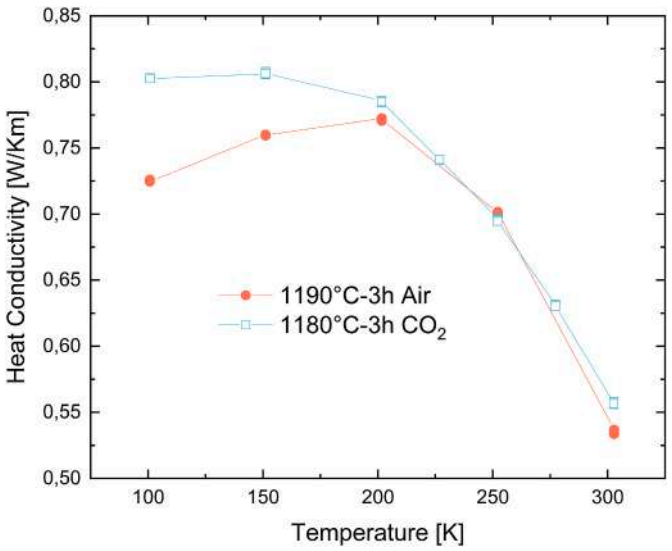

Fig. 12. Temperature dependence of the thermal conductivity of the LIS 1190°C-3h air sintered and the LIS 1180°C-3h sample sintered under simulated Martian atmosphere.

Table 5
Processing route and compressive strength of unfired samples produced using LIS and SC additive manufacturing methods, comparison with dry pressing.

Sample	Used dispersion medium	Used binder	Relative Density	Compressive strength
LIS [this study]	MSW	-	53.8%	0.93 ± 0.2 MPa
SC [this study]	MSW	-	60.4%	2.44 ± 0.46 MPa
SC [13]	DW + PC67	-	58.1%	3.34 ± 0.22 MPa
Dry pressed [13]	-	-	68.4%	1.64 ± 0.08 MPa
Hand build [13]	DW + PC67	-	62.4%	3.91 ± 0.23 MPa
Robocasting [13]	DW + PC67	-	63.4%	7.55 ± 1.33 MPa
LSD [13]	DW + PC67	Polymeric (5 wt%)	61.7%	30.8 ± 2.47 MPa

compared with the results of different wet additive manufacturing methods previously investigated [13]. Most of the wet processed green bodies characterized in the literature exhibit a compressive strength higher than dry pressed samples, while the highest values were reported for robocasting or layerwise slurry deposition specimens, albeit with the aid of a polymeric binder in the latter case [13]. These results, obtained with clay containing simulants, underline the importance of water and clays in the enhancement of particle rearrangement, agglomeration and formation of interparticle necks during drying. A detailed description of such phenomena can be found elsewhere [13]. Comparing the SC green bodies result with previous literature data reported in Table 5, a significant drop in compressive strength can be observed (−27%). Two factors can explain this outcome: firstly, the reduced clay content employed in this work (2.5 wt%) compared to the one used in Karl et al. [13] (5 wt%); secondly, the different dispersion medium, in the former, Martian Saltwater Simulant, while deionized water enriched with 0.5 wt % PC67 polymer was used in the latter. A halved clay content, while markedly reduces cracks during drying, also determines a decrease of the beneficial effects produced when wet processing this kind of material, i.e. clay swelling and ion dissolution-precipitation, believed to be responsible for the occurrence of strong bonds between unsintered particles [13].

In the case of LIS-printed green bodies, a further reduction of the compressive strength is primarily ascribable to the low densification level achieved (53.8%): high porosities are well known to affect mechanical performances negatively in regolith materials [46]. This outcome opens the possibility of further optimization studies of the LIS process aimed at obtaining higher relative densities in the unfired parts.

The compressive strengths relative to the 10 tested samples for each optimized sintering condition are reported in Supplementary Table S3, while the mean values are depicted as a bar chart in Supplementary Fig. S8. To identify statistically robust trends, the Weibull characteristic compressive strength [47] was evaluated and reported in Fig. 13. The same figure also evidences that the gap in the measured property between LIS (~100 MPa) and SC (~165 MPa) samples is maintained also after air sintering, reflecting their different densification level (i.e. 77.8 ± 3.1% vs. 84.2 ± 0.9%, respectively). However, density is not the only controlling aspect of mechanical performance in the samples processed in a simulated Martian atmosphere. Slightly lower Weibull characteristic compressive strengths of about 93 (LIS) and 151 MPa (SC) were obtained, while the achieved densification level accounted for 82.1 ± 3.3 and 82.7 ± 1.6%, respectively. Regarding the possible contribution of phase transitions on mechanical properties, the following considerations can be made. Magnetite formation could play a favourable role to promote LIS samples densification under simulated martian atmosphere (Fig. 9), as reported for cements and geopolymers [44]. However, comparing only the samples produced under optimized conditions, similar porosity levels and Magnetite content are displayed. Therefore, neither densification nor composition can be considered responsible for the observed differences in their mechanical properties. On the other hand, the following additional factors could play a role in this regard.

The first one is the difference in pore size between LIS and SC samples (Supplementary Table S2) Porosity features, whose role in regoliths was discussed in detail in a recent work [46], characterize LIS samples in terms of their bigger pore size, which is known to negatively affect mechanical properties [48,49]. The second feature is related to, as described previously, the intrinsic layered structure of LIS specimens (Fig. 5b). Indeed, layer-layer interfaces make LIS parts less resistant, resulting in a dependence of mechanical properties on the testing direction, as it was recently observed for other LIS-printed materials [27].

Since failure of brittle materials such as rocks [50] or MGS-1 sintered regolith [40] is reported to be due to axial fracture, compressive strength tests conducted in this work were carried out, as a conservative approach, along the direction parallel to the layers. Accordingly, the axial failure of LIS samples along the direction of weak layer-layer interfaces occurred at lower loads, with respect to SC ones.

Based on the results obtained in this work and literature data, it is possible to state that the techniques employed in this study allowed for the obtainment of superior compressive strengths for the sintered samples with respect to most previous studies carried out on consolidated Martian regolith [10,51–57], as reported in Fig. 14. In particular, composites of 80 wt% regolith - 20 wt% polyethylene produced by Sen et al. [51] showed compressive strengths of about 40 MPa. Sulfur concretes prepared by mixing 50 wt% sulfur with JSC Mars-1A simulant at about 120 °C, achieved a compressive strength above 50 MPa [52]. In another study, when 30 wt% sulfur was mixed with MGS-1 simulant, a value of 27 MPa was obtained [53]. Similarly, geopolymers fabricated starting from Martian regolith simulants and various additives showed compressive strengths of 55.27 [54] or 62.8 MPa [55]. Based on these investigations, where the aggregate bonding approach was employed, values up to around 27-63 MPa were obtained with this method so far (Fig. 14). Another study involves sintering of MGS-1 simulant enriched with about 5 wt% polyvinyl alcohol at 1150 °C, which led to samples with compressive strength of about 40 MPa, providing valuable insights on sintering mechanisms and compressive strength failure mode of Martian regoliths [40]. Recently, approaches aimed at maximizing the use of locally available materials have been also pursued [56–59].

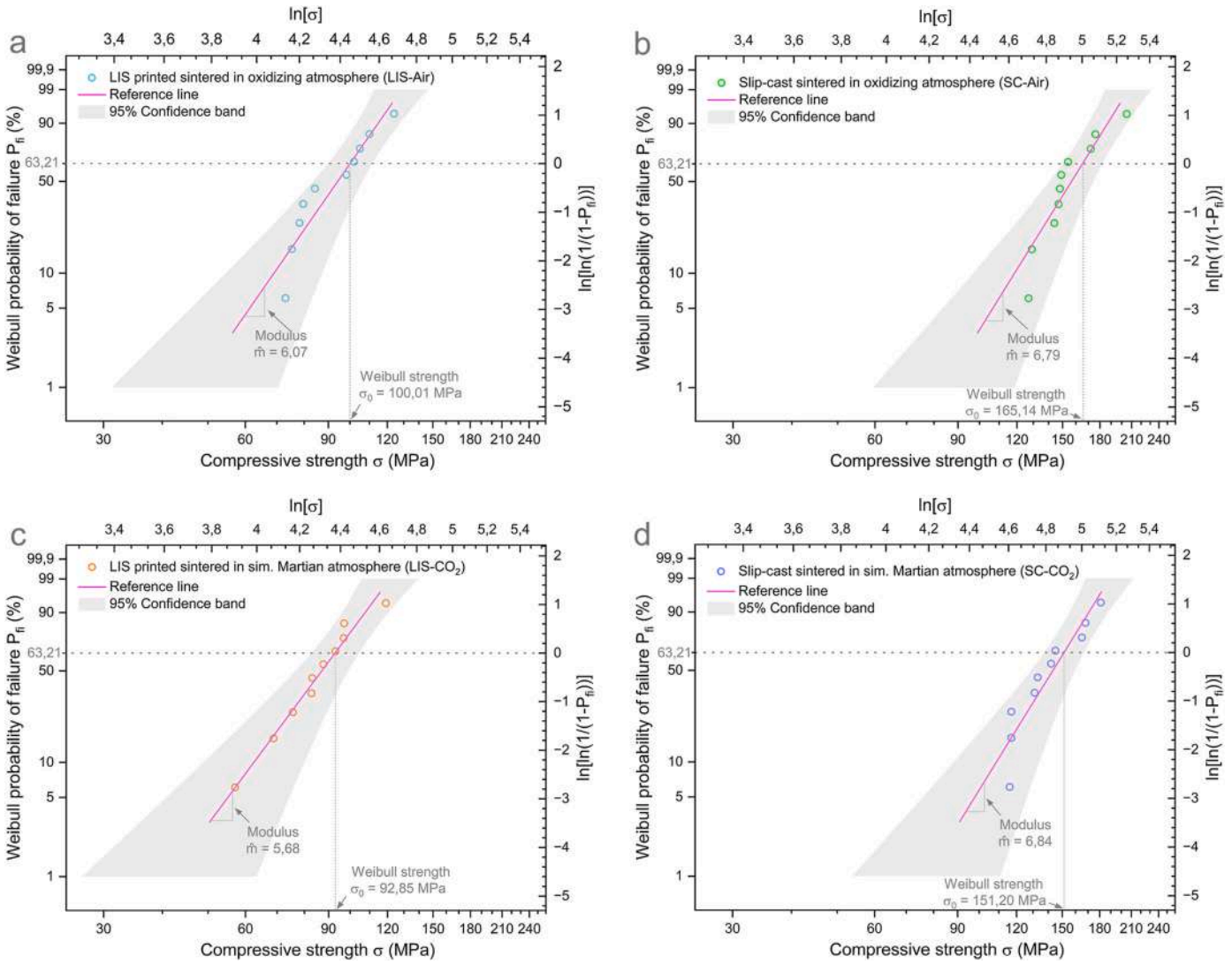

Fig. 13. Weibull fracture probability plots of the compressive strength measured for the cases of (a) LIS-AIR (LIS sample sintered in air at 1190°C-3h), (b) SC-AIR (SC sample sintered in air at 1190°C-3h), (c) LIS-CO_2 (LIS sample sintered in simulated Martian atmosphere at 1180°C-3h), (d) SC-CO_2 (SC sample sintered in simulated Martian atmosphere at 1180°C-3h).

Vibrational compaction of MGS-1, followed by sintering at 1150 and 1200 °C for 30 min, resulted in compressive strengths of ~27–77 MPa [56]. Cold sintering of a 5 wt% clay containing a mixture of MGS-1 and MGS-1C at 400 MPa with 10M NaOH provided compressive strength of 43 MPa, for 87.5% dense samples [57]. It should be noted that, despite the higher relative density achieved starting from similar materials, superior mechanical properties are attained in the present work. Recently, the Spark Plasma Sintering (SPS) technology enabled to achieve very promising compressive strength values [58,59]. Specifically, Min [58] reported values of about 103 and 137 MPa after sintering MGS-1 and JEZ-1 Martian regolith simulants, respectively. Even superior properties are reported in Casu et al. [59], i.e. about 310, 141, 152, and 198 MPa for JSC-Mars-1A, MMS, MGS-1 and JEZ-1 sintered simulants. This outcome can be readily justified by the very high densification levels attained (up to >99.9%). It is worth noting that even if the values obtained by SPS are similar or better than the ones achieved in this work, this technique appears unsuitable for the fabrication of complex shapes in one step [59].

It is important to state that, while higher compressive strength are obtained in this study via conventional SC, the time, cost and automation advantages described in the Introduction make LIS technology very promising in the framework of ISRU construction technologies. Furthermore, since LIS samples have been tested in their most sensitive direction, their compression performances can be considered lower estimates. Further optimization strategy of such process should involve the reduction of residual porosity and pore size in the LIS printed parts. The possible exploitation of the anisotropic nature of their layered structure could be also explored for future applications.

As reported in Fig. 14, the use of 100% in-situ available materials highlights the results of this study, suggesting that saltwater possibly present on Mars' crust is well suited to be used as a dispersion medium in wet-based additive manufacturing technologies.

4. Conclusions

The innovative Laser-Induced Slip Casting (LIS) technology has been tested in this work for the additive manufacturing of Martian regolith structures, starting from 100% in-situ available materials. A Martian saltwater simulant (MSW), based on Phoenix lander findings, has been employed as a dispersion medium in the fabrication of a 50 wt% solid loading slurry based on MGS-1 and MGS-1C Martian regolith simulants. After characterization in terms of rheology, processability and particle size, LIS technology and traditional slip casting were employed for additive manufacturing, obtaining green bodies with relative densities of

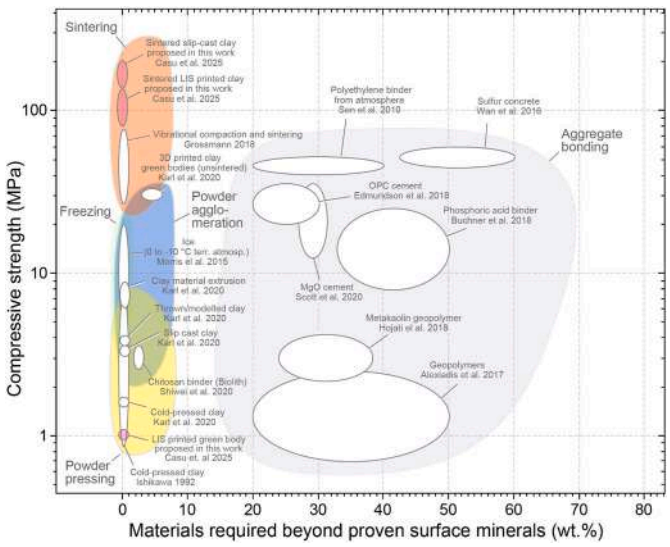

Fig. 14. Comparison of compressive strength over materials required beyond proven surface minerals of different studies that employed Martian regolith simulants. Image reworked with open access permission (CC-BY). For the detailed bibliographic citations of the referenced articles, see Karl et al. [10].

53.8% and 60.4%, respectively. Such green bodies were characterized in terms of their thermal stability, composition and compressive strength, showing modest mechanical performances of 0.9 (LIS) and 2.4 MPa (SC). On the other hand, when sintering was optimized according to different holding temperatures, first in an air and then in a simulated Martian atmosphere, samples showed peak compressive strengths of about 101 MPa (LIS) and 165 MPa (SC), overcoming most of the present literature findings in the Martian regolith consolidation framework. During sintering, phase transitions associated with vitreous phase crystallization, carbonates and sulfates decomposition, and Hematite and Magnetite formation have been observed, reflecting changes in the samples' color and magnetic behavior.

The obtained results demonstrate that, after proper optimization, no impairing effect is caused either by the use of Martian saltwater as a slurry dispersion medium or by sintering under simulated Martian conditions, underlying the transferability of the proposed approach to future Martian missions. LIS technology, even if further tunable and adaptable to the proposed Martian employment, represents a valid option in terms of both the obtained material performances and the possibility of scaling up and automate the process, if compared to traditional techniques such as slip casting.

CRediT authorship contribution statement

Mariano Casu: Writing – review & editing, Writing – original draft, Visualization, Methodology, Investigation, Funding acquisition, Formal analysis, Data curation, Conceptualization. **Jonathan Bahr:** Writing – review & editing, Visualization, Software, Investigation, Formal analysis. **Rafael Kleba-Ehrhardt:** Writing – review & editing, Resources, Methodology. **Thomas Mühler:** Writing – review & editing, Resources, Methodology, Investigation. **Martin Schwentenwein:** Writing – review & editing, Resources, Methodology, Conceptualization. **Ralf Feyerherm:** Writing – review & editing, Visualization, Software, Methodology, Investigation, Formal analysis, Data curation. **Roberto Orrù:** Writing – review & editing, Supervision, Resources, Project administration, Funding acquisition. **Giacomo Cao:** Writing – review & editing, Supervision, Resources, Project administration, Investigation, Data curation. **Aleksander Gurlo:** Writing – review & editing, Visualization, Supervision, Resources, Project administration, Methodology, Funding acquisition. **David Karl:** Writing – review & editing, Writing – original draft, Visualization, Supervision, Resources, Project administration, Methodology, Investigation, Funding acquisition, Conceptualization.

Declaration of competing interest

The authors declare that they have no known competing financial interests or personal relationships that could have appeared to influence the work reported in this paper.

Acknowledgments

Mariano Casu performed his activity in the framework of the Ph.D. in Innovation Sciences and Technologies at the University of Cagliari, Italy. Mariano Casu acknowledges the Deutscher Akademischer Austauschdienst (DAAD) for the awarded scholarship in the program Research Grants - Short-Term Grants, 2024. The authors thank Huaiyou Chen for the FTIR spectra, Delf Kober for the TG and MS data acquisition and Chenggui He for SEM, all at TU Berlin. The contribution of Lithoz GmbH and QEP3D GmbH to LIS printing is greatly acknowledged. The open-access funding was made possible through ProjektDEAL.

Appendix A. Supplementary data

Supplementary data to this article can be found online at https://doi.org/10.1016/j.ceramint.2026.03.213.

References

[1] J. Vago, O. Witasse, H. Svedhem, et al., ESA ExoMars program: the next step in exploring Mars, Sol. Syst. Res. 49 (2015) 518–528, https://doi.org/10.1134/S0038094615070199.
[2] K.A. Farley, K.H. Williford, K.M. Stack, et al., Mars 2020 mission overview, Space Sci. Rev. 216 (2020) 142, https://doi.org/10.1007/s11214-020-00762-y.
[3] Y. Zou, Y. Zhu, Y. Bai, et al., Scientific objectives and payloads of Tianwen-1, China's first Mars exploration mission, Adv. Space Res. 67 (2) (2021) 812–823, https://doi.org/10.1016/j.asr.2020.11.005.
[4] M. Smith, D. Craig, N. Herrmann, et al., The Artemis program: an overview of NASA's activities to return humans to the Moon, in: 2020 IEEE Aerospace Conference, Big Sky, 2020, pp. 1–10, https://doi.org/10.1109/AERO47225.2020.9172323. MT, USA.
[5] SpaceX, Mars and beyond: the road to making humanity multiplanetary. https://web.archive.org/web/20250224234951/https://www.spacex.com/humanspaceflight/mars. (Accessed 7 March 2025).
[6] G.B. Sanders, M. Duke, et al., Capability road map (CRM) 13: in-situ resource utilization (ISRU), in: R. Willcoxon, H. Thronson, G. Varsi, R. Mueller, V. Regenie, T. Inman, et al. (Eds.), NASA Capability Roadmaps Executive Summary, 2005, pp. 264–291. https://ntrs.nasa.gov/citations/20050204002. (Accessed 29 May 2024).
[7] K.M. Cannon, D.T. Britt, Feeding one million people on Mars, New Space 7 (2019) 245–254, https://doi.org/10.1089/space.2019.0018.
[8] A. Goulas, R.A. Harris, R.J. Friel, Additive manufacturing of physical assets by using ceramic multicomponent extra-terrestrial materials, Addit. Manuf. 10 (2016) 36–42, https://doi.org/10.1016/j.addma.2016.02.002.
[9] M.Z. Naser, Extraterrestrial construction materials, Prog. Mater. Sci. 105 (2019) 100577, https://doi.org/10.1016/j.pmatsci.2019.100577.
[10] D. Karl, K.M. Cannon, A. Gurlo, Review of space resources processing for Mars missions: martian simulants, regolith bonding concepts and additive manufacturing, Open Ceramics 9 (2022) 100216, https://doi.org/10.1016/j.oceram.2021.100216.
[11] D. Karl, F. Kamutzki, P. Lima, A. Gili, T. Duminy, A. Zocca, J. Günster, A. Gurlo, Sintering of ceramics for clay in situ resource utilization on Mars, Open Ceramics 2 (2020) 100008, https://doi.org/10.1016/j.oceram.2020.100008.
[12] B.L. Ehlmann, C.S. Edwards, Mineralogy of the martian surface, Annu. Rev. Earth Planet Sci. 42 (2014) 291–315, https://doi.org/10.1146/annurev-earth-060313-055024.
[13] D. Karl, T. Duminy, P. Lima, F. Kamutzki, A. Gili, A. Zocca, J. Günster, A. Gurlo, Clay in situ resource utilization with Mars global simulant slurries for additive manufacturing and traditional shaping of unfired green bodies, Acta Astronaut. 174 (2020) 241–253, https://doi.org/10.1016/j.actaastro.2020.04.064.
[14] A.M. Bramson, S. Byrne, N.E. Putzig, S. Sutton, J.J. Plaut, T.C. Brothers, J.W. Holt, Widespread excess ice in Arcadia Planitia, Mars, Geophys. Res. Lett. 42 (2015) 16, https://doi.org/10.1002/2015GL064844.
[15] P.D. Archer Jr., H.B. Franz, B. Sutter, et al., Abundances and implications of volatile-bearing species from evolved gas analysis of the Rocknest aeolian deposit, Gale Crater, Mars, J. Geophys. Res.: Planets 119 (1) (2014) 237–254, https://doi.org/10.1002/2013JE004493.
[16] N.O. Rennó, B.J. Bos, D. Catling, et al., Possible physical and thermodynamical evidence for liquid water at the Phoenix landing site, J. Geophys. Res. 114 (2009) E1, https://doi.org/10.1029/2009JE003362.

[17] A. McEwen, C.M. Dundas, S.S. Mattson, A.D. Toigo, L. Ojha, J.J. Wray, M. Chojnacki, S. Byrne, S.L. Murchie, N. Thomas, Recurring slope linae in equatorial regions of Mars, Nat. Geosci. 7 (2014) 53–58, https://doi.org/10.1038/NGEO2014.
[18] F.J. Martín-Torres, M.-P. Zorzano, P. Valentín-Serrano, Transient liquid water and water activity at Gale crater on Mars, Nat. Geosci. 8 (2015) 357–361, https://doi.org/10.1038/ngeo2412.
[19] D.L. Nuding, R.D. Davis, R.V. Gough, M.A. Tolbert, The aqueous stability of a Mars salt analog: instant Mars, Journal of Geophysical Research Planets 120 (3) (2015) 588–598, https://doi.org/10.1002/2014JE004722.
[20] D. Karl, F. Kamutzki, A. Zocca, O. Goerke, J. Guenster, A. Gurlo, Towards the colonization of Mars by in-situ resource utilization: slip cast ceramics from Martian soil simulant, PLoS One 13 (2018) e0204025, https://doi.org/10.1371/journal.pone.0204025.
[21] D. Linne, R. Moses, G. Sanders, J. Kleinhenz, R. Mueller, Mars ISRU & civil engineering current thinking and approaches, Presentation to the International Mars Exploration WorkingGroup (IMEWG), October 3, 2019, Oslo, Norway, https://ntrs.nasa.gov/citations/20200000010 (Accessed 20 February 2025).
[22] C. Buchner, R.H. Pawelke, T. Schlauf, A. Reissner, A. Makaya, A new planetary structure fabrication process using phosphoric acid, Acta Astronaut. 143 (2018) 272–284, https://doi.org/10.1016/j.actaastro.2017.11.045.
[23] P. Warren, N. Raju, H. Ebrahimi, M. Krsmanovic, S. Raghavan, J. Kapat, R. Ghosh, Effect of sintering temperature on microstructure and mechanical properties of molded Martian and Lunar regolith, Ceram. Int. 48 (2022) 35825–35833, https://doi.org/10.1016/j.ceramint.2022.07.329.
[24] A. Zocca, J. Günster, Towards a debinding-free additive manufacturing of ceramics: a development perspective of water-based LSD and LIS technologies, Open Ceramics 19 (2024) 100632, https://doi.org/10.1016/j.oceram.2024.100632.
[25] J. Lüchtenborg, T. Mühler, F. Léonard, J. Günster, Laser-induced slip casting (LIS) – a new additive manufacturing process for dense ceramics demonstrated with Si_3N_4, J. Ceram. Sci. Technol. 8 (4) (2017) 531–540, https://doi.org/10.4416/JCST2017-00091.
[26] J. Günster, J. Heinrich, T. Mühler, Method for Laser-Induced Additive Production of a Green Body by Means of Slip Casting, 2018 patent US20180141235A1.
[27] C.L. Cramer, M. Mohammadi, J.P. Feldbauer, D. Sabezki, M. Schwentenwein, E. Cakmak, M.J. Lance, M.K. Kidder, M.C. Martinez, S.M. Allan, B.L. & Armstrong, Laser-induced slip casting as an additive manufacturing approach for silicon carbide, J. Eur. Ceram. Soc. 46 (3) (2026) 117867, https://doi.org/10.1016/j.jeurceramsoc.2025.117867.
[28] J. Malaiškienė, R. Mačiulaitis, Frost resistant ceramics produced from local raw materials and wastes, Procedia Eng. 57 (2013) 739–745, https://doi.org/10.1016/j.proeng.2013.04.093.
[29] K.M. Cannon, D.T. Britt, T.M. Smith, R.F. Fritsche, D. Batcheldor, Mars global simulant MGS-1: a Rocknest-based open standard for basaltic martian regolith simulants, Icarus 317 (2019) 470–478, https://doi.org/10.1016/j.icarus.2018.08.019.
[30] Exolith Lab, Now Space Resource Technologies, Datasheet for MGS-1 Mars Global Simulant, University of Central Florida, USA, https://sciences.ucf.edu/class/simulant_marsglobal (Accessed 19 February 2025).
[31] Exolith Lab, Now Space Resource Technologies, Datasheet for MGS-1C Clay ISRU, University of Central Florida, USA, https://sciences.ucf.edu/class/simulant_mgs1c (Accessed 19 February 2025).
[32] H.G. Sizemore, M.T. Mellon, Laboratory characterization of the structural properties controlling dynamical gas transport in Mars-analog soils, Icarus 197 (2008) 606–620, https://doi.org/10.1016/j.icarus.2008.05.013.
[33] S. Gražulis, D. Chateigner, R.T. Downs, A.F.T. Yokochi, M. Quirós, L. Lutterotti, E. Manakova, J. Butkus, P. Moeck, A. Le Bail, Crystallography open database - an open-access collection of crystal structures, J. Appl. Crystallogr. 42 (4) (2009) 726–729, https://doi.org/10.1107/S0021889809016690.
[34] T.J. Collins, ImageJ for microscopy, Biotechniques 43 (sup1) (2007), https://doi.org/10.2144/000112517.
[35] A.P. Dhupe, A.N. Gokarn, Studies in the thermal decomposition of natural siderites in the presence of air, Int. J. Miner. Process. 28 (3–4) (1990) 209–220, https://doi.org/10.1016/0301-7516(90)90043-X.
[36] L. Tian, A. Tahmasebi, J. Yu, An experimental study on thermal decomposition behavior of magnesite, Journal of Thermal Analysis and Calorimetry 118 (2014) 1577–1584, https://doi.org/10.1007/s10973-014-4068-9.
[37] K.S.P. Karunadasa, C.H. Manoratne, H.M.T.G.A. Pitawala, R.M.G. Rajapakse, Thermal decomposition of calcium carbonate (calcite polymorph) as examined by in-situ high-temperature X-ray powder diffraction, J. Phys. Chem. Solid. 134 (2019) 21–28, https://doi.org/10.1016/j.jpcs.2019.05.023.
[38] B. Souza, R. Souza, I. Santos, E. Brocchi, $MgSO_4$ carbothermic reductive decomposition to produce a highly reactive MgO powder, J. Mater. Res. Technol. 9 (2) (2020) 1847–1855, https://doi.org/10.1016/j.jmrt.2019.12.017.
[39] M.N. Scheidema, P. Taskinen, Decomposition thermodynamics of magnesium sulfate, Ind. Eng. Chem. Res. 50 (2011) 9550–9556, https://doi.org/10.1021/ie102554f.
[40] N. Gupta, V. Dawara, A. Kumar, K. Viswanathan, Synthetic space bricks from lunar and Martian regolith via sintering, Adv. Space Res. 74 (8) (2024) 3902–3915, https://doi.org/10.1016/j.asr.2024.06.045.
[41] J. Oh, D. Noh, The reduction kinetics of hematite particles in H_2 and CO atmospheres, Fuel 196 (2017) 144–153, https://doi.org/10.1016/j.fuel.2016.10.125.
[42] V.P. Ponomar, O.B. Brik, Y.I. Cherevko, V.V. Ovsienko, Kinetics of hematite to magnetite transformation by gaseous reduction at low concentration of carbon monoxide, Chem. Eng. Res. Des. 148 (2019) 393–402, https://doi.org/10.1016/j.cherd.2019.06.019.
[43] D.J. Dunlop, Magnetic hysteresis of magnetite, pyrrhotite and hematite at high temperature, Geophys. J. Int. 225 (1) (2021) 1–14, https://doi.org/10.1093/gji/ggaa569.
[44] R. de Jesus Andrade Fidelis, M. Pires, D.S. de Resende, G.F. Costa Lima, P.R.P. de Paiva, A.C. Bezerra da Silva, Magnetite: properties and applications – a review, J. Magn. Magn Mater. 614 (2025) 172770, https://doi.org/10.1016/j.jmmm.2025.172770.
[45] I. Asadi, P. Shafigh, Z.F.B.A. Hassan, N.B. Mahyuddin, Thermal conductivity of concrete – a review, J. Build. Eng. 20 (2018) 81–93, https://doi.org/10.1016/j.jobe.2018.07.002.
[46] V. Dawara, N. Gupta, A. Dey, A. Kumar, K. Viswanathan, Pore–microcrack interaction governs failure in bioconsolidated space bricks, Ceram. Int. 48 (23) (2022) 35874–35882, https://doi.org/10.1016/j.ceramint.2022.09.013.
[47] A.C. Fischer-Cripps, Introduction to Contact Mechanics, Springer US, 2007, https://doi.org/10.1007/978-0-387-68188-7.
[48] A. Fakhimi, E. Alavi Gharahbagh, Discrete element analysis of the effect of pore size and pore distribution on the mechanical behavior of rock, Int. J. Rock Mech. Min. Sci. 48 (1) (2011) 77–85, https://doi.org/10.1016/j.ijrmms.2010.08.007.
[49] C. Lu-ping, X. Zu-qiang, J. Xue-long, W. Chun, Study on mechanical properties of rock like samples with prefabricated holes under specific temperatures, Sci. Rep. 15 (1) (2025) 42651, https://doi.org/10.1038/s41598-025-26738-y.
[50] A. Fakhimi, B. Hemami, Axial splitting of rocks under uniaxial compression, Int. J. Rock Mech. Min. Sci. 79 (2015) 124–134, https://doi.org/10.1016/j.ijrmms.2015.08.013.
[51] S. Sen, S. Carranza, S. Pillay, Multifunctional Martian habitat composite material synthesized from in situ resources, Adv. Space Res. 46 (2010) 582–592, https://doi.org/10.1016/j.asr.2010.04.009.
[52] L. Wan, R. Wendner, G. Cusatis, A novel material for in situ construction on Mars: experiments and numerical simulations, Constr. Build. Mater. 120 (2016) 222–231, https://doi.org/10.1016/j.conbuildmat.2016.05.046.
[53] K. Snehal, Priyanshu Sinha, Piyush Chaunsali, Development of waterless extra-terrestrial concrete using Martian regolith, Adv. Space Res. 73 (1) (2024) 933–944, https://doi.org/10.1016/j.asr.2023.07.036.
[54] L. Song, W. Lei, X. Zhu, L. Luo, Q. Wang, Microstructural and mechanical properties of high-strength geopolymer based on Martian soil simulant, Vacuum 230 (2025) 113753, https://doi.org/10.1016/j.vacuum.2024.113753.
[55] R. Shao, C. Wu, J. Li, Engineering cement-free high-performance Martian concrete with enhanced in-situ utilization of soil simulant: curing across −20 °C–40 °C and CO_2-rich environments, J. Environ. Manag., 375, 124426, https://doi.org/10.1016/j.jenvman.2025.124426.
[56] K. Grossman, Regolith-Based Construction Materials for Lunar and Martian Colonies, Supervisor: Sudipta Seal, University of Central Florida, Orlando, Dissertation, 2018. https://stars.library.ucf.edu/etd/6165. (Accessed 19 February 2025).
[57] L. Karacasulu, D. Karl, A. Gurlo, C. Vakifahmetoglu, Cold sintering as a promising ISRU technique: a case study of Mars regolith simulant, Icarus 389 (2023) 115270, https://doi.org/10.1016/j.icarus.2022.115270.
[58] T.J. Min, Manufacturing construction materials on Mars, A feasibility study on the use of spark plasma sintering (SPS) for bulk manufacturing of a viable ISRU Mars construction material using regolith simulant. Supervisor: Oğuzhan Copuroglu, Delft University of Technology, Dissertation, 2022. https://resolver.tudelft.nl/uuid:ed1f6110-c7f6-4103-b115-8b1675329c91. (Accessed 19 February 2025).
[59] M. Casu, R. Licheri, D. Bambas, F. Aymerich, L. Cappai, A. Concas, G. Cao, R. Orrù, Enhanced properties by spark plasma sintering of additive-free Martian soil simulants for ISRU applications, Ceram. Int. 51 (24) (2025) 42046–42058, https://doi.org/10.1016/j.ceramint.2025.06.423.